A study of the detection efficiency of the LIGO Interferometers to transient sources

by

Gautier Brunet

Submitted to the Department of Aeronautics and Astronautics
in partial fulfillment of the requirements for the degree of

Master of Science in Aeronautics and Astronautics

at the

MASSACHUSETTS INSTITUTE OF TECHNOLOGY
[June 2008]
February 2008

Author .....
Department of Aeronautics and Astronautics
January 2008

Certified by .....
Erotokritos Katsavounidis
Associate Professor of Physics
Thesis Supervisor

Certified by ....
.....
Paulo Lozano
Assistant Professor of Aeronautics and Astronautics
Thesis Supervisor

Accepted by .....
.....
David L. Darmofal
Associate Professor of Aeronautics and Astronautics
Chair, Committee on Graduate Students

A study of the detection efficiency of the LIGO Interferometers to transient sources

by

Gautier Brunet

Submitted to the Department of Aeronautics and Astronautics
on January 2008, in partial fulfillment of the
requirements for the degree of
Master of Science in Aeronautics and Astronautics

Abstract

The LIGO (Laser Interferometer Gravitational Wave Observatory) detectors have now completed their fifth science run and have reached design sensitivity. Gravitational wavebursts only last for a few cycles within the characteristic frequency band of LIGO.

This work focuses on the study of burst-like hardware injections during the fifth science run. Injected signals serve multiple purposes. Their primary goal is to study the cross-couplings between the gravitational wave channel and the auxilary channels. They also allow us to benchmark the ability of our search method to extract the signal parameters, thereby validating a whole portion of the analysis pipeline. Finally, they enable us to quantify the efficiency of our detectors depending on the strength and morphology of the signal. The stationarity of this parameter is also studied to ensure the variation of the sensibility is limited. Using theoretical estimations of the amplitude of the gravitational waves emitted by different sources, these efficiencies in turn allows us to have an estimate of the rate at which detection can be expected for each type of astrophysical object.

This work does not reflect the scientific opinion of the LIGO Scientific Collaboration and it was not reviewed by the collaboration.

Thesis Supervisor: Erotokritos Katsavounidis
Title: Associate Professor of Physics

Thesis Supervisor: Paulo Lozano
Title: Assistant Professor of Aeronautics and Astronautics

Acknowledgments

This work would not have been possible without the help and support from a lot of people in the Burst Analysis Group of the Ligo Scientific Collaboration. In particular I would like to thank Laura Cadonati, Michele Zanolin, Lindy Blackburn, Jared Markowitz, Leo Stein, Fred Donovan and Marie Woods for their assistance. I solicited their help countless times and I am very grateful for their availability and generosity.

I would also like to thank David Shoemaker for initially receiving me in the LIGO Laboratory and helping me find the right thesis topic.

Professor Katsavounidis is the single person without whom this would obviously have been impossible. I am very thankful for his trust and confidence. His support and guidance helped me a lot when I was lost in the long road of graduate research.

I would like to thank the LIGO Scientific Collaboration and LIGO for allowing the data and injections to be used and analyzed. I would also like to point out that this thesis is based on my work and does not in any way constitute an official LSC result.

Contents

List of Figures

List of Tables

Chapter 1

Introduction

The quest for gravitational waves is a recent scientific adventure. One of the predictions of Albert Einstein's General Relativity Theory is that a changing mass and energy distribution can create ripples in space-time which propagate away from the source at the speed of light. Their amplitude is so small that many, including Einstein himself, thought that they would remain for ever unverifiable theoretical predictions.

Even if gravitational waves have never been detected directly, their indirect influence has been measured in the binary neutron star system PSR1913+16 [1]. In this binary, one of the star is a pulsar that emits radio waves at an extremely stable frequency. The observation of the variation in the time of arrival of radio pulses allows us to compute the orbital parameters of the binary. The observed loss of potential gravitational energy measured by the decreasing distance between the two objects is equal within measurements error to the theoretical rate predicted by General Relativity.

Throughout the sixties, however, Joseph Weber struggled to detect them using massive aluminum cylinders [2]. His pioneering work in resonant mass detectors has led to the development of the more sophisticated and sensitive interferometers.

Today, the Laser Interferometer for Gravitational wave Observation (LIGO) has completed its five science runs and accomplished its sensitivity goals [3]. Similar efforts are being undertaken in Europe - with GEO and Virgo - and Japan - with

TAMA and LCGT. Even if no detection has been made yet, extremely valuable information has been gained in order to move on to the next step on th road to detection and observation. Indeed, detector sensitivity increased from one science run to the other and the data being analyzed now is the most promising to date.

Furthermore, advanced LIGO, expected to start collecting data in 2013, could very well be the first instrument to detect a wave. Its reach will be multiplied by an order of magnitude. This means that detection will be 1000 times more likely to occur in a given observation time.

In Chapter 2, we explain the basics of gravitational wave detection. We start by describing the potential sources of such waves and by explaining the theory of gravitational wave propagation and detection. We then describe the LIGO detectors, and try to understand the fundamental limitations that these interferometers have in detecting gravitational waves.

In Chapter 3, we describe the burst search pipeline. We start by looking at how the injections are performed and describe the algorithm that searches for candidate events.

In Chapter 4, we study the results of the analysis of the data, including the parameter estimation and the efficiency calculations. We verify the coherence of these results with the information on the noise levels and translate these efficiencies in detection range and probability. Finally, we look at wether these results are stationnary throughout and after the fifth science run.

We conclude in Chapter 5 by summarizing the significance of this work and outline potential future investigations.

Chapter 2

Gravitational radiation

2.1 Sources

The first idea one has in order to study gravitational waves is to generate them in a laboratory. A simple calculation of the order of gravitational wave magnitude that a rotating dumbbell, a high energy accelerator or a nuclear explosion could create clearly proves that waves of astronomical origins are by far those we are the most likely to detect. Burst waveforms can be generated by a number of sources [4], [5] and [6].

2.1.1 Neutron Star Binaries

A binary star is a stellar system consisting of two stars orbiting around their center of mass. Unfortunately, binaries emit at a very low frequency and will remain out of reach for some time.

However, as we have seen for PSR1913+16, the emission of waves progressively over millions of years increases the frequency of emission as the stars come closer together. The signal emitted will resemble a chirp in that the frequency and amplitude will increase as the two objects coalesce. This signal will be characterized by the masses radial separation and eccentricity of the two orbiting bodies. The end of life of a neutron star binary could emit copious amounts of gravitational waves at

frequencies up to 1 kHz.

2.1.2 Supernovae

Type II supernovae are triggered by the violent collapse of a stellar core to form a neutron star or a black hole. According to [7], gravitational waves from such sources may be detectable throughout our galaxy and the Magellanic Clouds.

2.1.3 Pulsars

Pulsars are believed to be highly magnetized rotating neutron stars which emit a beam of radio waves. Their periods range from 1.5 ms to 8.5 s. The radiation can only be observed when the beam of emission is pointing towards the Earth. The gravitational wave emission would result from the rotation of the presumably nonaxisymmetric neutron star. Uncertainty in the ellipticity of those objects prevents us from predicting the levels of emission.

2.1.4 Black holes

After a star of sufficient mass has undergone a supernova explosion, it sometimes retains sufficient mass to continue to collapse. The mass collapses past the mathematical boundary known as the event horizon, a boundary past which gravitational attraction around the mass is so strong that not even light can escape, and continues to condense until the mass is crushed into a point of zero dimension known as a singularity.

The calculation of gravitational wave emission from black holes is somewhat challenging, as is the calculation of wave emission from supernovae. Calculation of the emission from a falling test particle has been found to depend on the respective masses of the test particle and the black hole, as well as the angular momentum of the particle orbiting the black hole as it falls inward. A similar calculation can be performed for two black holes falling into one another. Since light does not escape from a black hole, gravitational radiation may be the most effective method of observation, since

information about the gravitational attraction around the black hole, and hence the matter inside, can be found from the waves emitted.

2.1.5 Stochastic background

Similar to the cosmic microwave background and the unprobed cosmic neutrino background, density fluctuations in the early universe can lead to a stochastic background of gravitational waves . If this signal is ever detected it could give us extremely valuable information on the early universe, possibly as early as the Planck time. It would indeed potentially allow us to discriminate different cosmological models. However, for most models the predicted amplitude of the stochastic background is well below the sensitivity of what is technologically achievable today or in the intermediate future.

2.1.6 Serendipitous science

As always when inventing a new way of looking at things, unsuspected phenomena might very well turn out to be dominant.

Our goal is to search for - and characacterize the detector efficiency to - all possible signals, as long as they have short duration and a frequency content in the 64-1600 Hz band which stands out above the detetor noise. This is why on top of astrophysical signals like the Zwerger-Muller waveform, "ad-hoc" waveforms with Gaussian and sine-Gaussian morphologies were injected (see 3.1 for details). Similar sensitivities may be expected fo different waveforms with similar overall characteristics (central frequency, bandwidthn duration). See [8] and [9] for a detailed discussion on the extent to which this statement is true.

2.2 Gravitational wave theory

Gravitational waves are ripples in the curvature of spacetime. Their theoretical existence is a consequence of Einstein's General relativity. They are the vector of gravitational information when a body changes its gravitational attributes. Contrary to Newton's theory where the information on the masses is instantly known everywhere, these waves propagate out from their source at the speed of light.

In this chapter we will describe the theoretical construction without pretending to prove anything. For a complete treatment see [4], [10], [11] and [12].

Space time interval ds between two points is given by the Minkowski metric of Special Theory of Relativity by:

$$ds^2 = -c^2dt^2 + dx^2 + dy^2 + dz^2 \tag{2.1}$$

or

$$ds^2 = g_{\mu\nu}\, dx_\mu\, dx_\nu \tag{2.2}$$

For small perturbations to a flat space-time, $g_{\mu\nu}$ can be written as the sum of $\eta_{\mu\nu}$ and $h_{\mu\nu}$ where $\eta_{\mu\nu}$ is the unperturbed metric and $h_{\mu\nu}$ is the metric perturbation.

$$g_{\mu\nu} = \eta_{\mu\nu} + h_{\mu\nu} \tag{2.3}$$

In the transverse traceless gauge, in which coordinates are marked out by the lines of free falling test masses, the weak field limit of Einstein's field equation becomes a wave equation:

$$\left(\nabla^2 - \frac{\partial^2}{\partial t}\right) h_{\mu\nu} = 0, \tag{2.4}$$

and $h_{\mu\nu}$ takes the form:

$$h_{\mu\nu} = \begin{pmatrix} 0 & & & \\ & h_+ & h_X & \\ & h_X & -h_+ & \\ & & & 0 \end{pmatrix}$$

h+ and h correspond to the two orthogonal polarizations of the gravitational waves. Their respective effect on a circle when passing orthogonally to the page is illustrated below:

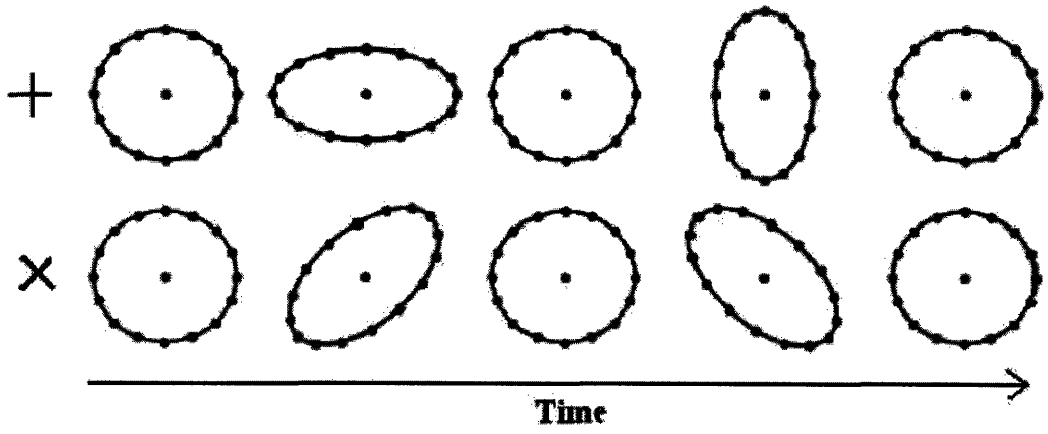

Figure 2-1: The evolution of the shape of an otherwise circular arrangement of free masses as a wave passes orthogonally to the plane defined by the arrangement. This evolution is shown for both polarizations. Time passes from left to right.

Lastly, we define the root-sum-square amplitude of a gravitational wave as:

$$h_{rss} = \sqrt{\int_{-\infty}^{+\infty} h(t)^2 \, dt}. \tag{2.5}$$

2.3 LIGO interferometers

The effect of a wave is to stretch and shrink objects in orthogonal directions.

One way to determine with precision the distance between objects is to measure the time it takes for light to travel from one object to the other. The earliest use of light to experimentally determine the nature of spacetime is Michelson and Morley's interferometric experiment. There are two complementary approaches to detect gravitational waves with laser interferometers: space-based and earth-based. A space-based antenna is free from seismic excitations and can utilize long arm lengths of order 10^{10} m. It is best suited to detect gravitational waves in a frequency band between 10^{-4} Hz and 10^{-1} Hz.

An earth-based antenna has its best sensitivity in a frequency band between 100 Hz and 1000 Hz. The Laser Interferometer Gravitational Wave Observatory, or LIGO [13], is made up of three such interferometers. Two are colocated in Hanford in Washington State. One, referred to as H1, is 4 km long. The second, H2, is 2 km long. The LIGO Livingston Observatory in Louisiana has a single interferometer with 4 km arms, called L1.

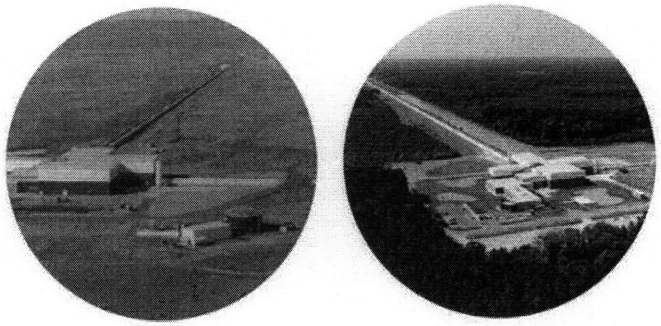

Figure 2-2: The two LIGO interometers

2.3.1 Antenna Pattern

The detector does not have the same response to waves coming from any direction. Let x and y be the directions defined by the interferometer arms. If a wave arrives from the x or y direction, the displacement will only happen in the other arm. The sensitivity is therefore half of what it is when coming from the z direction with the proper polarization. Similarly, if a wave arrives along the bisector between the x and y axes, the change in length will be equal in both arms, generating no difference in the travel times of the laser.

The response to a wave arriving at local time t depends on the dimensionless amplitude and polarization and its arrival direction [14]. In the low frequency limit, the differencial strain signal detected by the interferometer can be expressed as the projection of two polarization components.

$$h_{det} = F_+(\alpha, \delta, t)h_+(t) + F_\times(\alpha, \delta, t)h_\times(t) \tag{2.6}$$

where α and δ are the right ascension and declination of the source.

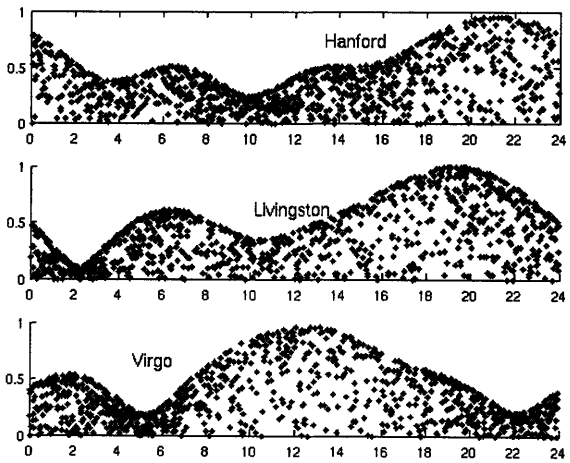

Figure 2-3: Evolution of the F_+ component as a function of time when looking at waves with random polarizations coming from the center of the galaxy ($\alpha = 17h45m40.04s$, $\delta = -2900'28.1"$). The factors are different from one site to the other because the interferometers are oriented differently.

These plots allow us to predict when the three detectors are the most sensitive to waves coming from a given direction.

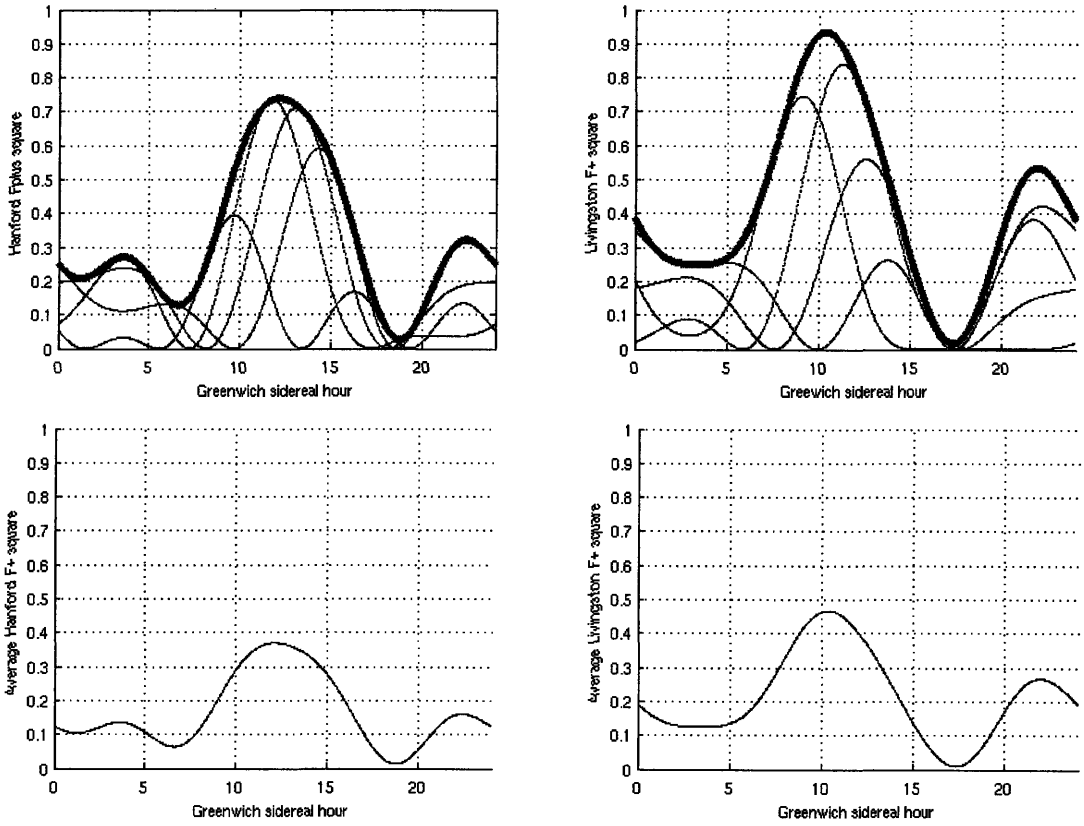

Figure 2-4: The two first graphs show the F_+^2 component of a linearly polarized wave coming from Scorpius X-1 for four different polarizations 0, 30, 45 and 60 degrees. The lower two graphs show the polarization-averaged antenna pattern.

When looking at the sky from Earth, Scorpius X-1 is the strongest source of X-rays after the Sun. Recent theories predict a temporal correlation in the X-ray emissions and the gravitational radiation of this low mass X-ray binary.

Those graphs therefore allow us to predict the antenna pattern that shoud be expected when observing this source and consequently when the best time to observe it is.

2.3.2 Primary Noise Sources

LIGO has accomplished its five science runs and reached its performance goals. The last one, S5, started in November 2005 and ended in September 2007.

The sensitivity of the detectors is in fact primarily limited by three noise sources.

Under 40 Hz, seismic activity is the main noise source.

Thermal noise is dominant between 40 and 150 Hz and corresponds to thermal fluctuations in the mirror that can excite the fundamental pendulum mode.

Above 150 Hz, shot noise dominates. It is a result of photon counting statistics.

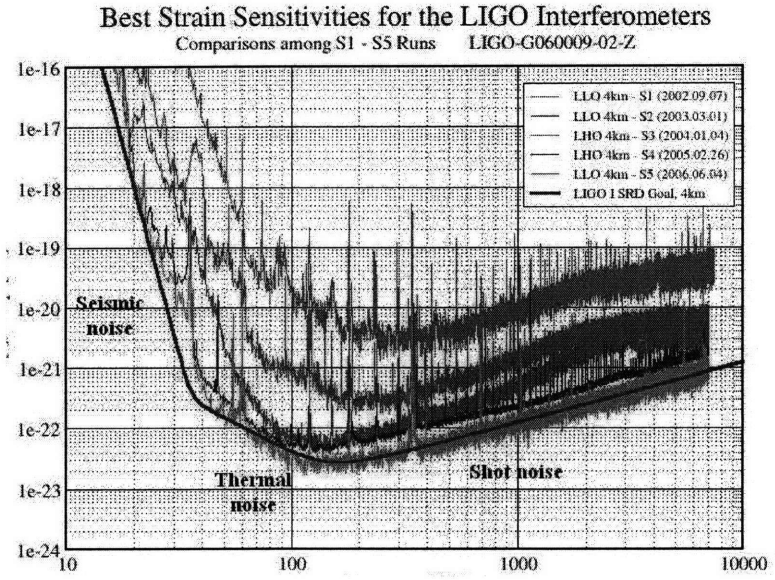

Figure 2-5: Best LIGO sensitivity curve as of June 4, 2006 with historical comparisons[1]. h[f] is defined such that the signal energy in a given frequency band is $\int h^2[f]df$.

The Science Requirements Document (SRD) [15] takes into account those three major noise sources.The S5 sensitivities achieve a performance comparable to the SRD goal. The difference corresponds to secondary noise sources. The 60 Hz comb is the result of coupling with the alternating current and all its harmonics. Moreover, daily human activity temporarily increases noise levels on a daily basis.

Chapter 3

Signal Hardware Injections and Burst Search Methods

So far the quest for these waves has remained an elusive goal. When the time we believe something was detected comes, the characteristics of the instruments need to be known well enough in order to prove that the trigger can not possibly be due to anything else. One way to characterize the instrument's response to a wave is to simulate one. Waveforms can be prepared in advance and injected in the detector. Adding the signals to the digitized time series that the detector recorded is called performing a software injections. Hardware injections are done by directly exciting the mirrors according to the simulated gravitational wave pattern.

In this work we will address only the hardware injections.

These injections were intended to address any instrumental issues, including calibrations, and provide a robust end-to-end test of LIGOs data analysis pipelines. They also provided an important tool for establishing the safety of the veto analysis, i.e., the absence of any couplings between a real gravitational wave burst and the auxiliary channels we considered as potential vetoes.

3.1 Hardware Injections

In order to understand the response and performance of the LIGO interferometers, we inject signals and study the response of the detector and the analysis pipeline. The exact knowledge of the input allows us to confirm and predict the instrument's behavior. Hardware injections provide the only end-to-end test of the system.

3.1.1 S5 Hardware injections

The hardware injections can be classified in two categories.

The daily burst injections were made to characterize the detector and therefore have strengths above and below the 50 % efficiency hrss. The waveforms injected include:

- *Sine-Gaussians*: sinusoid with a given frequency inside a Gaussian envelope with Q= 9, and f_0 assumed the value of 70, 235, 914 and 2000 Hz.

  $h(t_0 + t) = h_0 sin(2\pi f_0 t) exp(-\frac{(2\pi f_0 t)^2}{2Q^2})$

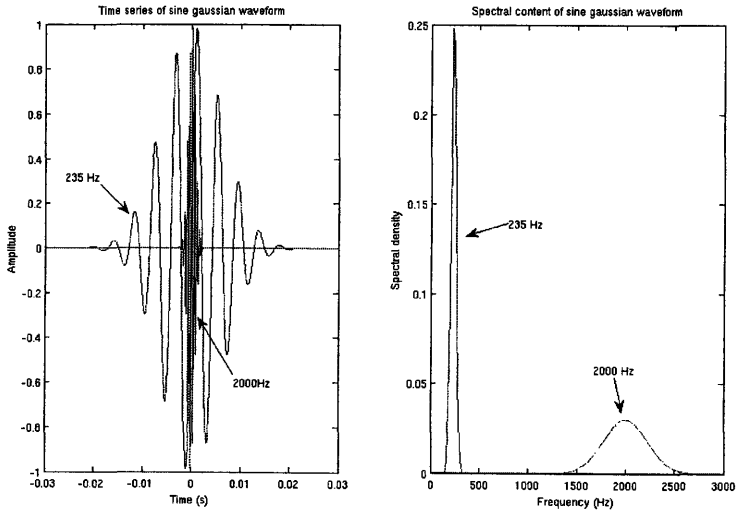

Figure 3-1: Time series and spectral content of two sine-Gaussian waveforms with Q=9: 235 and 2000 Hz.

- *Zwerger-Mueller waveforms* resulting from numerical simulations of core collapse supernovae, A3B3G1. Refer to [16] for a comprehensive analysis.

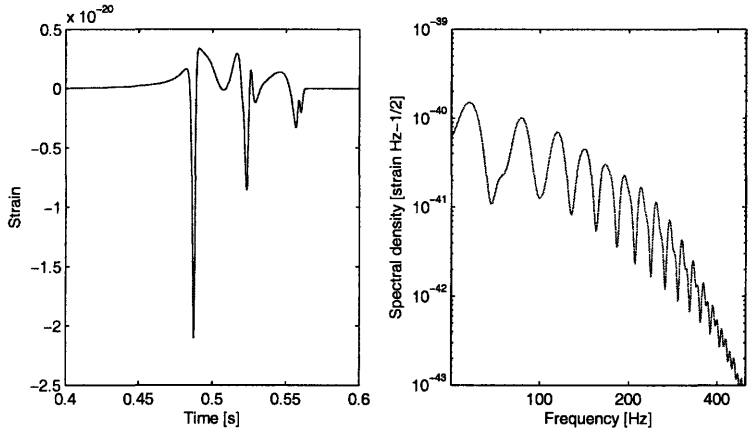

Figure 3-2: Time series and spectral content of a Zwerger Muller waveform.

- *Gaussians* of the form $h(t_0 + t) = h_0 * exp(-\frac{t^2}{\tau^2})$ with τ equal to 1 ms. On the following plot we have also included Gaussian waveforms with the time constants corresponding to the strong injections. It allows us to observe the impact of that parameter on the waveform morphology and its spectral signature. In particular, as the time constant increases, most of the signal power is under 100 Hz and the performance of our search method decreases (see 4.2.1 Gaussian Waveforms).

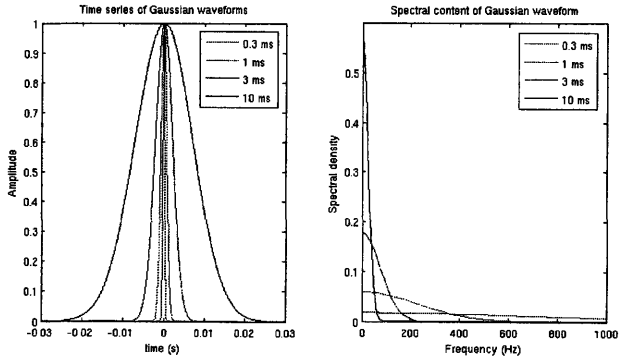

Figure 3-3: Gaussian waveform characteristics.

- *Cosmic string cusps* with a cutoff frequency of 220 Hz. Refer to [17] for more details.

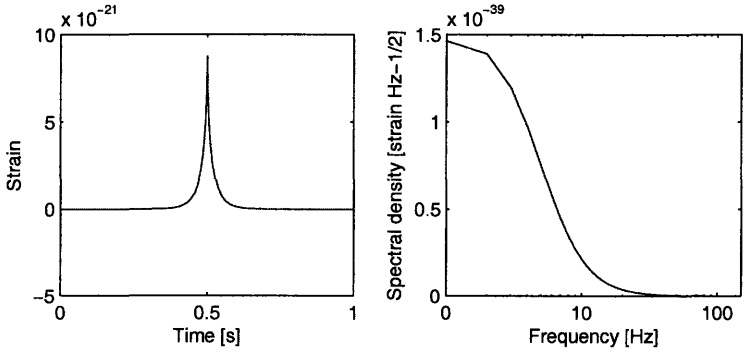

Figure 3-4: Cosmic Cusps waveform characteristics.

- *Band-limited white noise burst (wnb250bw100dt30)* These have a specified central frequency of 250 Hz and bandwidth of 100 Hz and have a Gaussian envelope in the time domain with a sigma of 30 ms.

  They have two polarization components so the incident waveforms at Hanford and Livinsgton were chosen to be different.

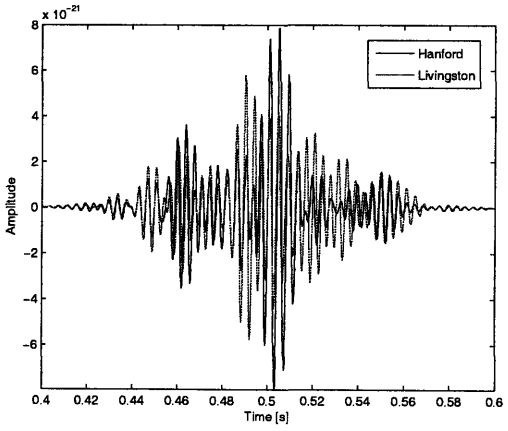

Figure 3-5: Time series of the white noise waveform for Hanford and Livingston. The white noise waveform is the only one for which the injected waveform is different from one site to the other.

- *Ringdown waveform.* The final state of a compact binary coalescence is expected to be a perturbed black hole which will radiate away the perturbations as gravitational waves in the form of a damped sinusoid [18]. The waveform that we used corresponded to a f_0 of 2600 Hz and a decay time of 300 ms.

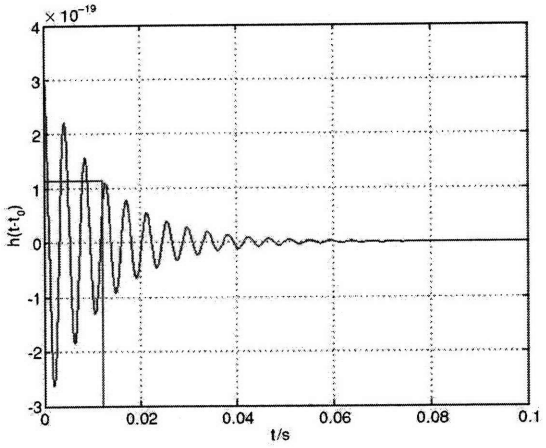

Figure 3-6: Ringdown waveform from a black hole of mass 100 M⊙ and spin 0.96 corresponding to a f_0 of 235 Hz and Q = 9, at a distance of 1 Mpc.

The sine-Gaussian and Gaussian waveforms were chosen to represent the two general classes of short-lived gravitational wave bursts of narrow-band and broad-band character respectively. The supernovae and binary black hole merger waveforms were adopted as a more realistic model for gravitational wave bursts.

High amplitude bursts were also injected. These have two amplitudes, roughly 16 and 32 times the threshold of detectability. They consist of:

- Sine-Gaussians with Q=9 at a ten different frequencies: 50, 70, 100, 153, 235, 393, 554, 850, 1304, 3068 Hz.

- Loud Gaussians with tau= 0.3, 1, 3 and 10 ms.

A total of 20 different waveforms we injected during the S5 run. The injections were grouped in sets whose magnitude were varied. The injections were not performed on a fixed schedule.

Injected Waveform	H1	H2	L1
Gaussian 0.3 ms	90	94	72
Gaussian 1 ms	1208	1438	1078
Gaussian 3 ms	90	94	72
Gaussian 10 ms	90	94	72
sine-Gaussian 50 Hz	78	92	62
sine-Gaussian 70 Hz	1182	1433	1077
sine-Gaussian 100 Hz	88	103	64
sine-Gaussian 153 Hz	88	103	64
sine-Gaussian 235 Hz	1207	1450	1075
sine-Gaussian 393 Hz	78	92	62
sine-Gaussian 554 Hz	83	101	62
sine-Gaussian 850 Hz	78	92	62
sine-Gaussian 914 Hz	1104	1341	1015
sine-Gaussian 1304 Hz	88	103	64
sine-Gaussian 2000 Hz	1189	1422	1070
sine-Gaussian 3068 Hz	78	92	62
Band-limited White Noise, 250 Hz, $\delta f = 100Hz$, $\sigma = 30ms$	1104	1341	1015
Zwerger Muller (A3B3G1)	1114	1341	998
Cosmic String Cusps, f_{cutoff}=220 Hz	1090	1341	983
Ringdown 2600 Hz, $\delta t = 30ms$	178	198	143
Total	10305	12338	9172

Table 3.1: Number of S5 hardware injections on each detector. For all the sine-Gaussians, Q=9.

3.1.2 Hardware injections procedures

This section was largely inspired by the work of M. Sung. For more details, refer to [19]. The Gravitational Wave channel $DARM\_ERR$ is the error point of the interferometer differential arm-length feedback control loop, and is called $e(t)$. The actuators for this control loop are the end test mass coil actuators. The LIGO calibration group has utilized several independent techniques in efforts to attain the absolute calibration of the end test mass coil actuators [20].

The detected strain is the sum of the gravitational wave and the noise: $s(t) = n(t) + h(t)$. A(f) is the actuation function. It can be divided into the actuation performed on ETMX and ETMY, using the coupling coefficients k_x and k_y.

$$A(f) = k_x A_x(f) - k_y A_y(f) \tag{3.1}$$

Injections are performed on ETMX. In order to take into account the actuation function to the X arm, we divide the desired antenna strain waveform in the frequency domain, $h_{inj}(f)$ by $A_x(f)$:

$$a_x(f) = -h_{inj}(f)/A_x(f) \tag{3.2}$$

$a_x(f)$ is then transformed back to the time domain.

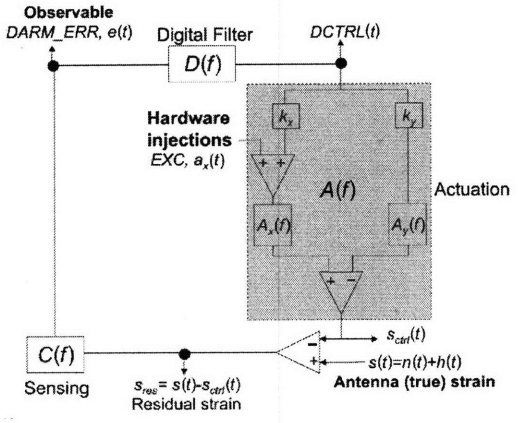

Figure 3-7: Simplified block diagram of the differential arm servo system of the LIGO detectors

C(f) and D(f), the sensing and digital filter blocks, are linear response functions that model the differential arm servo system. $e(f) = C(f)(s(f) - s_{ctrl}(t)) = C(f)(s(f) - A(f)D(f)e(f))$ so

$$s(f) = \frac{1 + C(f)D(f)A(f)}{C(f)} e(f) = R(f)e(f) \tag{3.3}$$

where R(f) is the response function of the detector.

An injection period starts 5 seconds before the first injection and ends 5 seconds after the last injection. The injection period is divided into 64 seconds segments with 16 seconds overlapping with the next segment. Noise spectrum is obtained from measurements 50 seconds before and after the injection period.

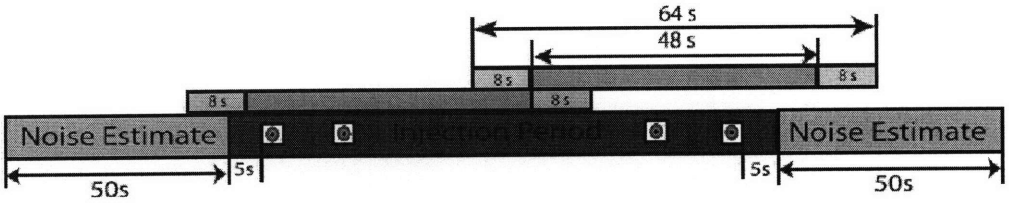

Figure 3-8: Time segmentation of the analysis

3.2 KleineWelle

The first stage of the burst search pipeline is to identify times when the GW channels of the three interferometers appear to contain signal power in excess of the baseline noise. These times are called triggers and can be generated using different algorithms. KleineWelle [21], [22] is the algorithm we will use in order to quantify the efficiency of the different detectors. KleineWelle is a time-frequency method utilizing multi-resolution wavelet decomposition. The time-frequency decomposition is obtained using the Haar wavelet transform.

The wavelet transform for a time series f(t) is defined by the integral:

$$G(u,s) = \int_{-\infty}^{+\infty} f(t) \frac{1}{\sqrt{(s)}} \Psi^* \left(\frac{t-u}{s} \right) dt \tag{3.4}$$

The squared wavelet coefficient provide an estimate of the energy associated with a certain time-frequency pixel.

For the case of discrete data, a computationally efficient algorithm exists for calculating wavelet coefficients over scales that vary as powers of two. This is the dyadic wavelet transform. The simplest example of such wavelets is the Haar function:

$$\Psi^{Haar}(t) = \begin{cases} 1 & 0 \leq t < 1/2 \\ -1 & 1/2 < \mathrm{t} \leq 1 \\ 0 & \text{otherwise} \end{cases}$$

Clustering is used to increase sensitivity and provide a normalized cluster energy. The significance of a cluster is defined as the negative logarithm of the probability that the energy result from gaussian white noise. A trigger is generated when this number exceeds a certain threshold.

Two versions of KleineWelle were used to produce the efficiency curves. One for the frequencies between 64 and 1024 Hz, the other for higher frequencies. This had an impact on certain properties of the parameter estimation (see Section 4.1.2. Frequency Reconstruction).

Chapter 4

Data Analysis of Signal Injections

4.1 Signal Parameter Estimation

Analysing the parameters of the response, namely the exact time of detection and the estimated frequency of the detected signal allows us to check the whole detection pipeline is functioning properly.

4.1.1 Timing

On top of verifying that KleineWelle is functionning properly, the timing distribution allows us to define a time window specific to each waveform. How close should the trigger be in order to postulate that the injection was detected? By looking at the histogram of the difference between the injection peak time and the closest trigger, one can differentiate detected signals from background triggers and deduce the time window that defines detection.

The central peak stands out from the background very clearly. We did check however that the histogram density outside the defined interval matched the average background rate, equal to the total number of triggers times the total number of injections when we substract the peak divided by the total observation time.

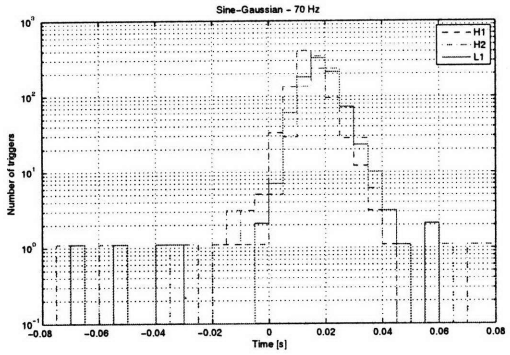

Figure 4-1: Timing error plot for the sine-gaussian waveform of 70 Hz. The distribution is more spread out for lower frequencies.

The time window necessary to include all the detected signals narrows as the frequency f of the signal increases. This is consistent with the fact that the time between two peaks in the signal scales as 1/f.

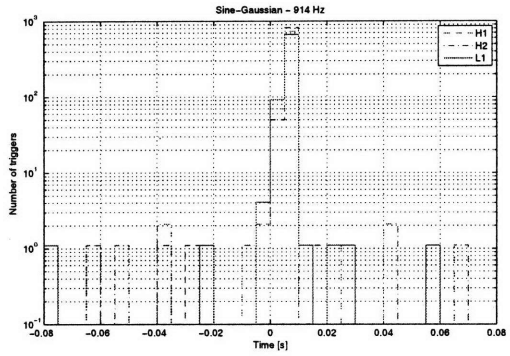

Figure 4-2: Timing error plot for the sine-gaussian waveform of 914 Hz. The peak is contained inside a time window of 15 ms that becomes the citerion for detection. The mean error is less than 4 ms and the standard deviation is around 3 ms for the three detectors. The constant deviation is due to the burst-finding algorithm data conditioning filters.

The following plot summarizes the results for all the waveforms. As mentioned earlier, the low frequency sine-Gaussians and the 10 ms second Gaussian waveform have less clean distributions. For all the other signals, the mean deviation is typically under 5 ms and the standard deviation under 3 ms.

		H1	H1	H2	H2	L1	L1
Δt	Waveform	Mean	S.D.	Mean	S.D.	Mean	S.D.
11	0.3 ms	8	0.4	7.5	0.5	7.5	0.6
20	1 ms	8	3.5	6.5	4.4	8.6	3.4
32	3 ms	17	3.8	14.4	2.4	14.5	2.9
75	10 ms	11	20.6	1.8	7.2	13.3	22.7
32	50 Hz	9	7.5	17.6	6.3	13	5.5
50	70 Hz	12	7.8	11.5	10.6	15.3	9.2
21	100 Hz	7	3.3	7.5	3.1	7.5	0.9
15	153 Hz	6	1.7	7	2.2	6.8	1.3
15	235 Hz	5	3.2	4	3.8	5	3.2
10	393 Hz	8	1.3	7.1	1.1	6.8	0.5
8	554 Hz	6	0.9	5.3	0.8	5.4	0.1
8	850 Hz	6	1	5.1	0.8	5.3	0.2
9	914 Hz	4	2.4	3.3	2.8	4.1	2.5
4	1304 Hz	1.7	0.7	1.7	0.7	2	0.4
5	2000 Hz	5	3.2	4	3.8	5	3.2
5	3068 Hz	8	1.3	7.1	1.1	6.8	0.5
20	White Noise	7	5.8	5	6.2	0.4	2.6
10	Zwerger Muller	-2	1.6	-1.5	2	-1	2
20	Cosmic Cusps	3	5	1.6	3.9	4	5.8

Table 4.1: Measure of the mean and standard deviation of the timing error of the detected injections. All times are in milliseconds. The Δt defining detection is determined by looking at the whole distribution and differentiating the distribution of detected signals from the background triggers.

4.1.2 Frequency Reconstruction

KleineWelle uses the powers of 2 in the frequency domain to define the time-frequeny pixels that it analyzes. Despite this intrinsically poor frequency resolution, it is interesting to quantify KleineWelle's performance at estimating frequency. Two versions of KleineWelle were used to produce these plot, for under and over 1024 Hz.

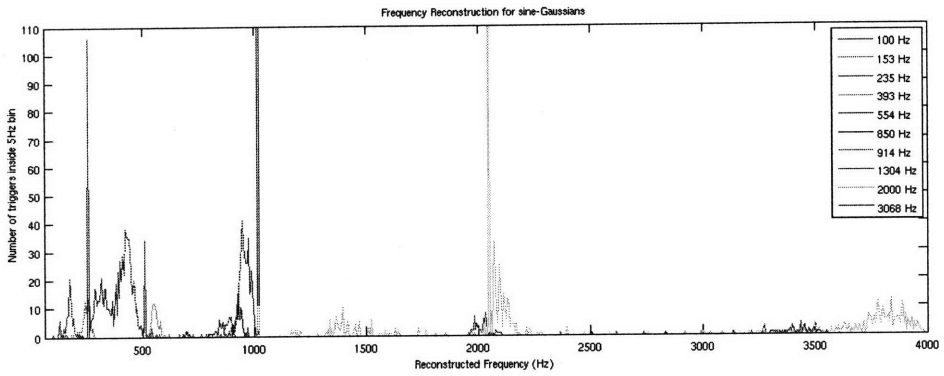

Figure 4-3: Distribution of the reconstructed frequency for each sine-gaussian waveform. The peak at 1024 Hz is due to the use of two versions of the algorithm.

The 100, 153, 393 and 850 have a small standard deviation, typically around 15 Hz. This constancy in the reconstructed frequency is due to the fact that these are high amplitude injections.

	H1	H1	H2	H2	L1	L1
Frequency (Hz)	Mean detected Frequency (Hz)	Standard Deviation (Hz)	Mean detected Frequency (Hz)	Standard Deviation (Hz)	Mean detected Frequency (Hz)	Standard Deviation (Hz)
100	176	14	173	12	168	13
153	253	13	247	20	248	10
235	384	88	382	98	368	81
393	558	14	567	17	550	17
554	862	59	903	41	844	63
850	934	13	938	12	942	10
914	986	88	996	71	989	65
1304	2075	184	2050	34	2018	35
2000	2570	636	2781	733	3151	940
3068	3259	589	3474	325	3336	236

Table 4.2: Mean reconstructed frequency and standard deviation of the detected injections for each interferometer

On the other hand, the daily injections - 235, 914 and 2000 Hz - give a more spread out distribution, beacause their amplitude is sometimes much smaller.

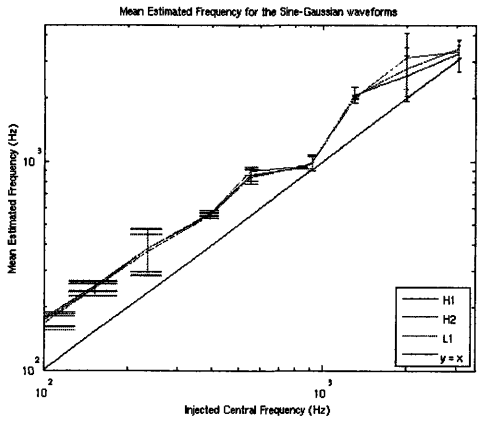

Figure 4-4: Mean Estimated frequency as a function of injected central frequency of the sinegaussian waveforms.

The low mean reconstructed frequency of the 914 Hz sine-Gaussian is another consequence of the use of two versions of KleineWelle.

Overall, KleineWelle has a tendency to over-estimate the frequency of the detected signal by a factor of 70 %. This is due to the logarithmic tiling of the KleineWelle analyis.

4.2 Efficiency curves

The following plots show the measured efficiency of the analysis pipeline as a function of root-sum-squared strain amplitude, e(h_{rss}), for each simulated waveform. The efficiency data points for each waveform are fit with a function of the form:

$$e(h_{rss}) = 1/(1 + \frac{h_{rss}}{h_{50\%}}^{\alpha(1+\beta tanh(\frac{h_{rss}}{h_{50\%}}))}) \tag{4.1}$$

where $h_{50\%}$ is the hrss corresponding to an efficiency of 0.5, α is the slope, β is the parameter that descries the asymetry of the sigmoid. This fitting function was adopted by the burst analysis group [23], [24] and [25],. One characteristic of all these plot is that H1 and L1 are on average 1.7 times more sensitive than H2, which is consistent with H2's smaller length of 2 km. H1 and L1 are indeed twice as long.

The analytic expressions of the fits are used to determine the signal strength h_{rss} for which the 50% efficiency is reached. These fits are subject to statistical errors from the limited number of injections. We will approximate these with Poisson error bars even if a proper treatment requires binomial distribution.

Also, the overall amplitude scale is subject to the uncertainty in the calibration of the interferometer response. This uncertainty was conservatively estimated to be 10% during the fourth science run [26].

4.2.1 Gaussian waveforms

The two graphs corresponding to 0.3 and 3 ms were not able to compute a sigmoid because the signals injected to study coupling effects were too loud to be able to determine efficiencies. The 10 ms Gaussian does not even have an efficiency of one at those high amplitudes because most of its power is under 100 Hz.

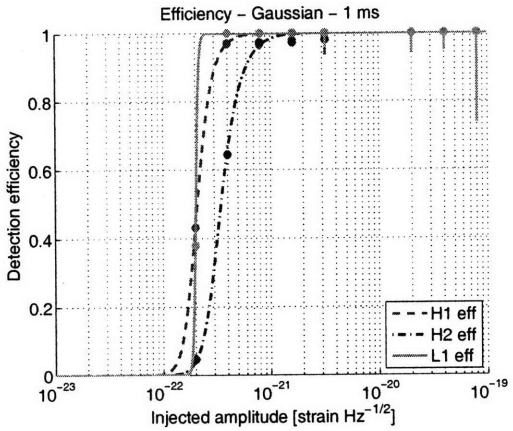

The L1 curve of the 1 ms Gaussian waveform is very steep. This is due to the fact that only one amplitude has an efficiency that is less than 1.

4.2.2 Sine-Gaussian waveforms

Here also it is obvious that some of these waveforms were injected for coupling studies, as their amplitudes are more than an order of magnitude above their threshold of detectability.

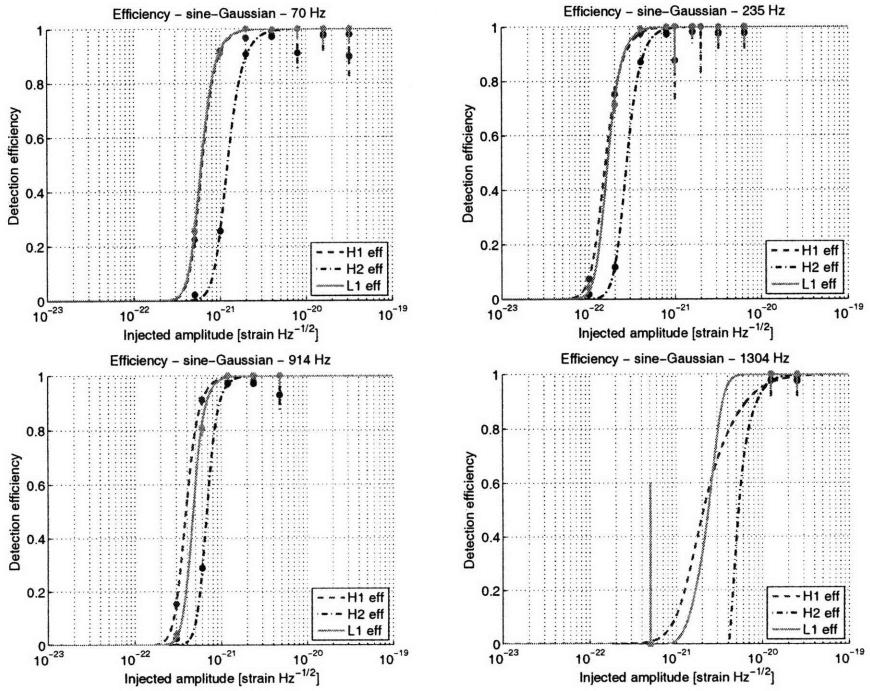

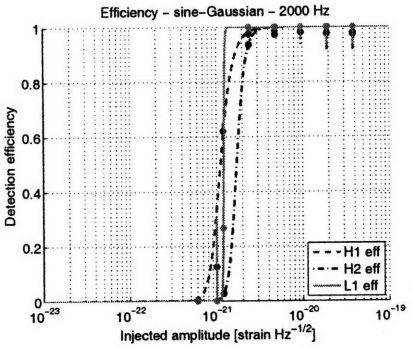

4.2.3 Astrophysical waveforms

For the Zwerger-Muller waveform, the L1 efficiency curve is once again abnormally steep for statistical resons. The L1 and H1 curves are actually supposed to be very close. L1 is surprisingly less sensitive than H1 to the white noise waveform. If the

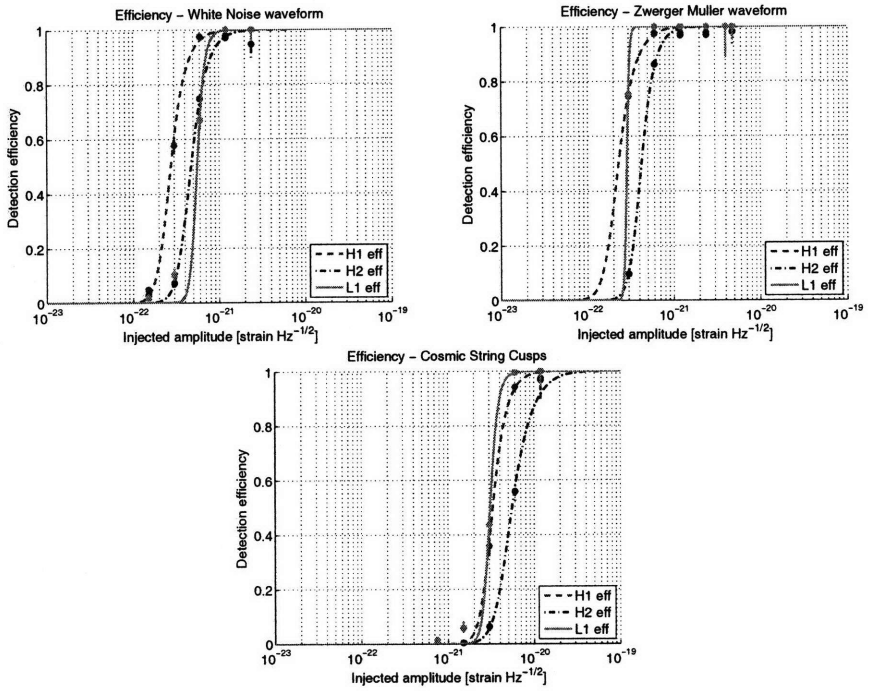

injected waveforms were identical, L1 should be closer to H1. This feature is constant throughout S5 (see section 4.4.) and does not correspond to a temporary drop in L1's sensitivity.

In fact the injected waveforms were chosen to be different for Hanford and Livingston.

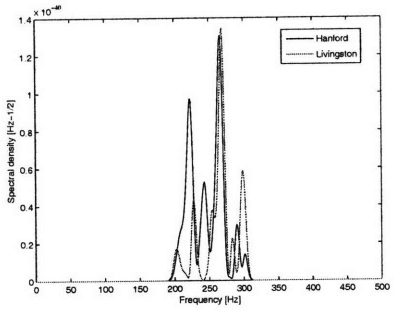

Figure 4-5: Spectral density of the white noise waveform for the two sites. The energy distribution for Hanford matches better the most sensitive frequency range of the detectors.

4.3 Signal to Noise Ratio considerations

For all of the Sinegaussians, the quality factor is fixed. The quality factor quantifies how damped the oscillations are. A high Q means that the system will oscillate many times before loosing its energy.

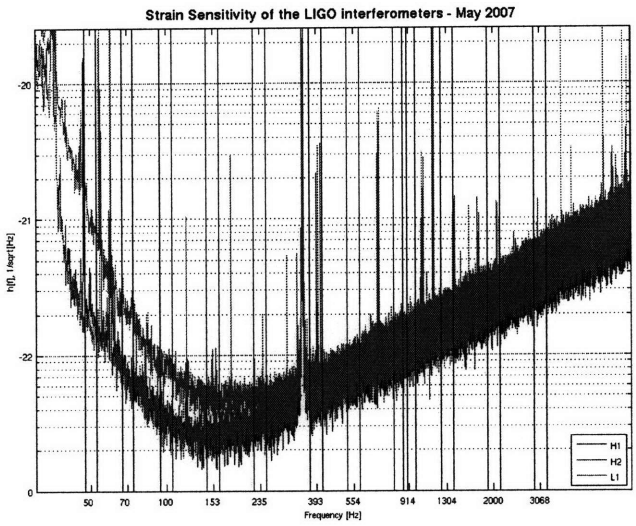

Figure 4-6: Strain sensitivity of the LIGO interferometers - May 2007

This graph shows the current noise levels [27]. The intervals have a constant width because the x-axis is logarithmic. This constant width is narrow enough for us to define a noise level. The values were chosen to represent the average value in the

interval. The following table shows those numbers.

The four sinegaussians in the daily burst injections, namely 70, 235, 914 and 2000 Hz were chosen to define the value of SNR 50 %.

	H1	H2	L1
sine-Gaussian 50 Hz	2.1	9	1.6
sine-Gaussian 70 Hz	0.65	1.9	0.7
sine-Gaussian 100 Hz	0.32	0.85	0.26
sine-Gaussian 153 Hz	0.22	0.47	0.27
sine-Gaussian 235 Hz	0.32	0.5	0.33
sine-Gaussian 393 Hz	0.45	0.7	0.49
sine-Gaussian 554 Hz	0.6	0.95	0.7
sine-Gaussian 850 Hz	0.9	1.4	1
sine-Gaussian 914 Hz	1	1.56	1.15
sine-Gaussian 1304 Hz	1.4	2.15	1.55
sine-Gaussian 2000 Hz	2.2	3.15	2.5
sine-Gaussian 3068 Hz	3.5	5.5	3.8

Table 4.3: Noise levels defined by figure 4.5. for each interferometer

Note that these averages are nearly constant from one interferometer to the other. The high values of the ratio for the 1304 Hz waveform is due to the poor fitting performance of the sigmoid curve.

	H1	H2	L1
sine-Gaussian 70 Hz	9.4	6.4	8.6
sine-Gaussian 100 Hz	8.8	7.4	9.6
sine-Gaussian 153 Hz	6.8	6.4	5.6
sine-Gaussian 235 Hz	4.9	5.5	5.2
sine-Gaussian 914 Hz	3.9	4.3	4.1
sine-Gaussian 1304 Hz	14.3	18.6	14.2
sine-Gaussian 2000 Hz	5.0	5.5	4.9

Table 4.4: Ratio of detection threshold and noise level

4.4 Comparison with software results

Software injections add a simulated signal to the data after it has been recorded. Since they performed this a posteriori, the interferometer is not affected while it is recording data.

Here we compare our efficiency results to those obtained by L.Blackburn using the S5 software injections.

The hardware injections are optimally oriented, while the software injections come from a randomized direction and have a randomized polarization. In order to account for that, we have multiplied the detection thresholds of the software results by the average antenna pattern. The value of the average antenna pattern is $\frac{1}{\sqrt{5}}$ for the direction and $\frac{1}{2}$ for the polarization. See [4] for details.

	H1 S	H1 H	H2 S	H2 H	L1 S	L1 H
sine-Gaussian 70 Hz	5.7	6.1	11.7	12.1	8.3	6.0
sine-Gaussian 100 Hz	2.2	2.7	4.4	6.3	2.9	2.5
sine-Gaussian 153 Hz	1.2	1.5	2.9	3.0	1.5	1.5
sine-Gaussian 235 Hz	1.4	1.6	2.8	2.8	1.6	1.7
sine-Gaussian 554 Hz	3.0	2.6	4.5	4.1	3.9	3.0
sine-Gaussian 850 Hz	3.5	3.8	6.3	6.0	8.2	4.3

Table 4.5: Comparison of hardware (H) and software (S) detection thresholds

We observe that they are remarkably similar.

The software results are on average 5 to 10 % smaller than the hardware results. One significant discrepancy is the value for L1 for the 70 Hz waveform. The two approaches agree on the Hanford detector's performance, but the software analysis reveals much weaker performance for L1 corresponding to a 50 % increase in the detection threshold.

4.5 Detection range

In order to have a better idea of what these sensitivities mean, we can convert it to spheres inside which an event of a given strength needs to happen in order to be detected. Here we follow the approach of [25].

$$\frac{d^2E_{GW}}{dAdt} = \frac{1}{16\pi} \cdot \frac{c^3}{G} \cdot < \dot{h}_+^2 + \dot{h}_x^2 > \tag{4.2}$$

For a high Q sine-Gaussian waveform of frequency f_0 emitted isotropically at a non-relativistic distance r, we obtain:

$$E_{GW} = \frac{r^2c^3}{4G} \cdot (2\pi f_0)^2 h_{rss}^2 \tag{4.3}$$

According to Ott et al. [28], a core-collapse supernova's waveform can be modeled by a high Q sine- Gaussian with a central frequency 654 Hz. A linear interpolation of our results gives us an $h_{50\%}$ of $3.10^{-22}Hz^{-1/2}$ at that frequency. Just like in [4], we take into account the fact that the waveform is not monochromatic, and that the fact that is spread in the time-frequency plane reduces the sensitivity by a factor of 2 and obtain a reach of 2 kpc for this model. The second estimation we can use is that of a binary black hole merger waveform calculated by the Goddard numerical relativity group [29]. The s25WW model, based on a 25 M$\odot$ progenitor; emits more energy in gravitational waves but with a higher characteristic frequency of 937 Hz. If we consider this similar to a high-Q sine- Gaussian, we obtain a reach of 100 kpc. According to [29], a binary system of two 10 M$\odot$ black holes will radiate up to 3.5% of its total mass and have a peak emission at 750 Hz. The reach obtained for those values is 22 Mpc. Similarly, if the mass of each black hole is 100 M$\odot$, the reach is 800 Mpc.

4.6 Variability of the efficiency

4.6.1 Throughout S5

The evolution of the efficiency was studied for the daily injections, as they are numerous enough to be cut up into quarters. The efficiency was found to be stable, in a satisfactory way. Below is the evolution of the efficiency of the 235 Hz sine-gaussian waveform. Apart from a slight L1 decrease in the first quarter, the curves barely evolve throughout S5.

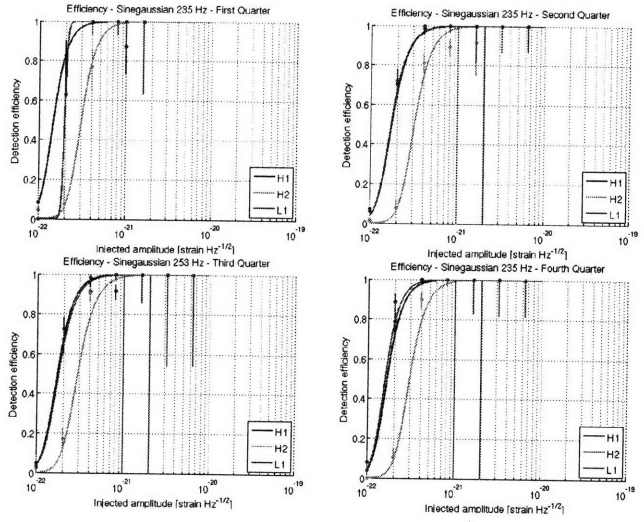

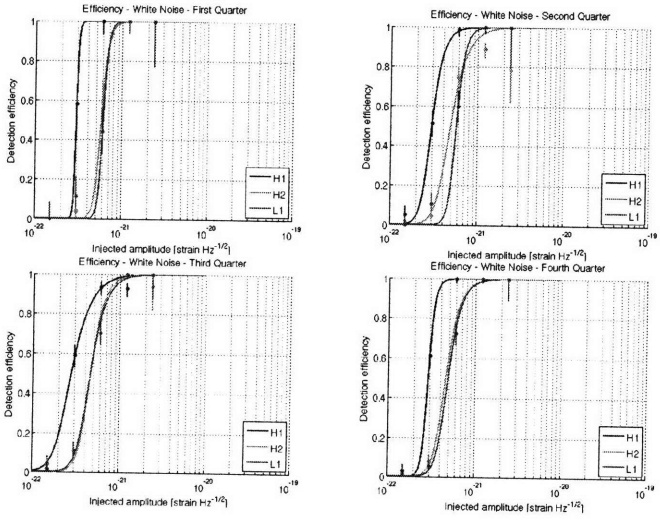

Similarly, the efficiency to the white noise waveform shows remarquable stability.

The relatively low L1 sensitivity to a white noise waveform is a constant feature throughout S5.

4.6.2 Post S5 studies

The fitting performance in the S5 efficiency curves was often limited by the distribution of the injected strengths. These plots indeed have more data points on the right of the threshold of detectability than on the left. Furthermore, these points were generally too spread out. On October 7th, we performed a series of hardware injections taking those remarks into account.

Injected waveform	H1	H2	L1
Gaussian 0.3 ms	600	635	587
Gaussian 1 ms	600	642	596
sine-Gaussian 70 Hz	580	614	556
sine-Gaussian 235 Hz	588	616	594
sine-Gaussian 914 Hz	428	450	434
sine-Gaussian 2000 Hz	612	632	589
sine-Gaussian 3068 Hz	579	615	571
Zwerger Muller (A3B3G1)	459	478	403
White Noise	457	485	440

Table 4.6: Number of post-S5 injections performed on October 7th 2007

The density of the injected hrss was doubled and the number of points on each side of the detection threshold was balanced (see appendix). The lower statistics of this series of injections is compensated by the better distribution of injected signal strengths.

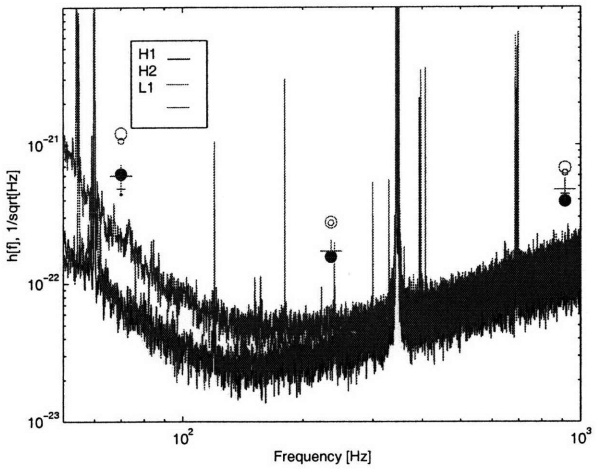

Figure 4-7: Detection efficiency on October 7th

The performance of the detector is generally better during the post S5 period by a factor of 14%. This is due to the continuous comissionning throughout the fifth science run. In fact the efficiency during the post S5 run is very similar to that at the end of S5. The discrepancy for the H1/L1 efficiencies at the end of the S5 run are again due to the unicity of the point with an efficiency that is different from 1.

The calibration uncertainty taken to be 10% [26] account for the smaller discrepancies. In fact, if we assume the same slope for H1/L1 and H2, we would obtain $2 * 10^{-22} Hz^{-1/2}$, a value that is much closer to the Post-S5 efficiencies.

Interferometer	H1			H2			L1		
Period	S5	End	Post-S5	S5	End	Post-S5	S5	End	Post-S5
Gaussian 1 ms	2.09	2.0	1.59	3.48	3.5	3.10	2.03	2.0	1.71
sine-Gaussian 70 Hz	6.15	5.5	4.42	12.15	11.5	10.73	6	5.5	4.84
sine-Gaussian 235 Hz	1.56	1.5	1.52	2.76	2.8	2.73	1.71	1.5	1.54
sine-Gaussian 914 Hz	3.90		3.94	6.79		6.23	4.73		4.40
Zwerger Muller	2.3	2.8	1.92	4.29	4.1	4.08	2.88	2.8	1.88
White Noise	2.79	2.7	2.36	4.77	4.6	4.43	5.61	5.0	3.62

Table 4.7: Comparaison of detection thresholds for various waveforms during, at the end of and after S5. The "End" period refers to the end of the S5 run.

Appendix A

Timing error

- Gaussian waveforms

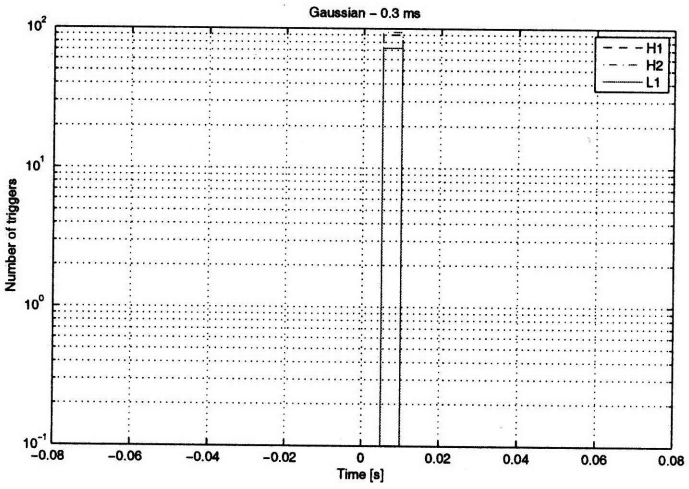

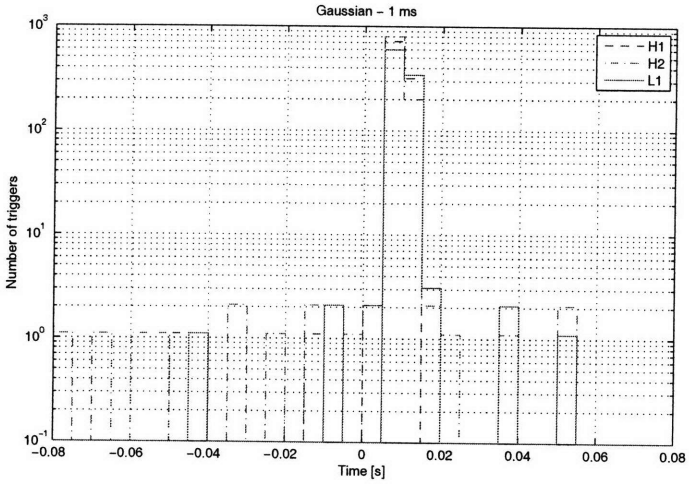
Gaussian – 1 ms
H1
H2
L1
Number of triggers
Time [s]

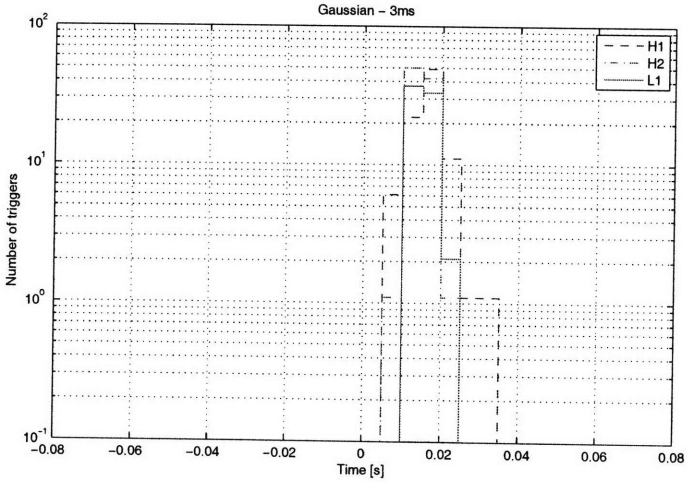
Gaussian – 3ms
H1
H2
L1
Number of triggers
Time [s]

- Sine-Gaussians waveforms

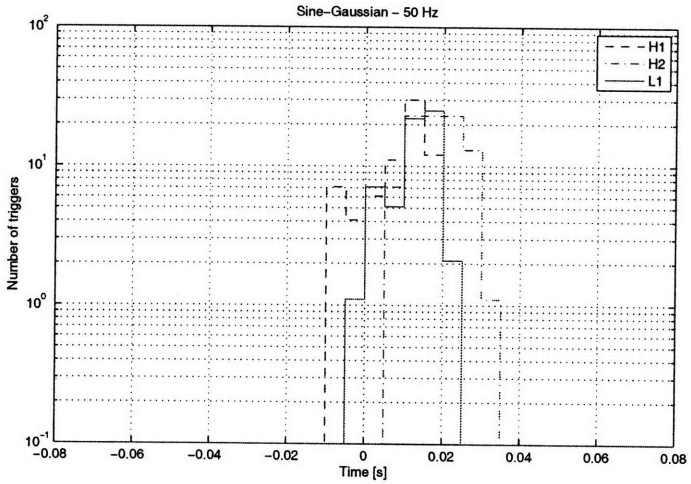

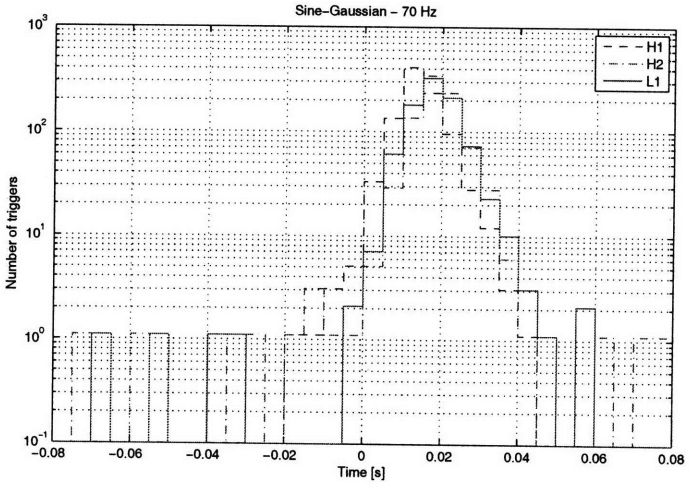

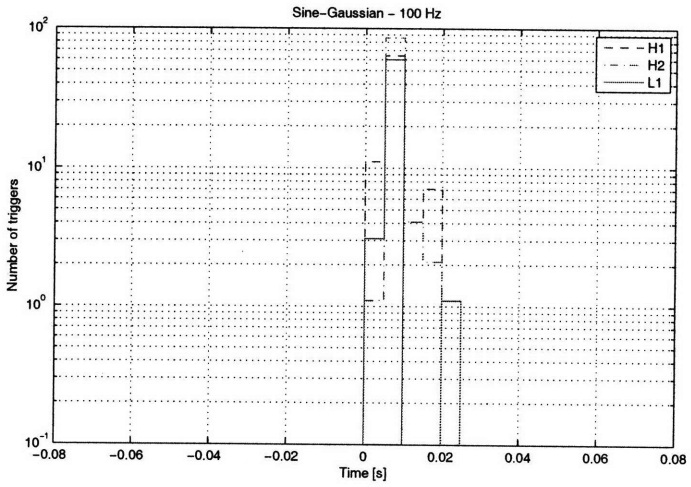
Sine–Gaussian – 100 Hz
H1
H2
L1
Number of triggers
Time [s]

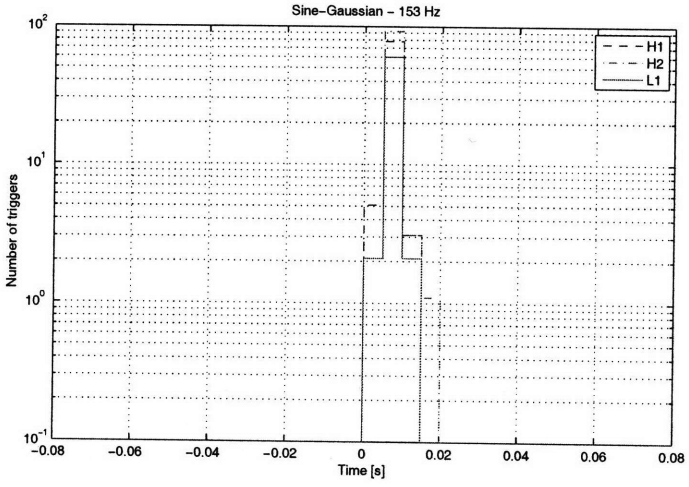
Sine–Gaussian – 153 Hz
H1
H2
L1
Number of triggers
Time [s]

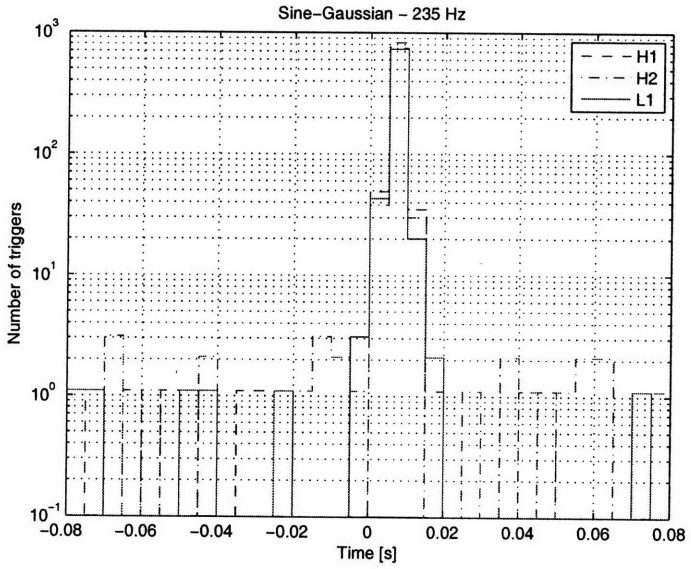
Sine–Gaussian – 235 Hz
H1
H2
L1
Number of triggers
Time [s]

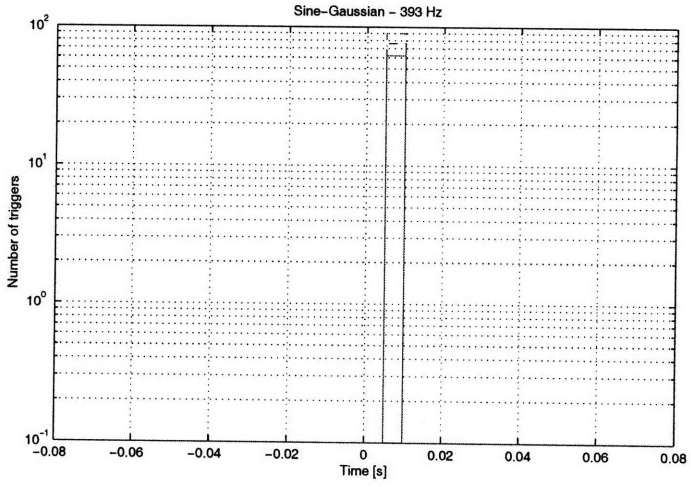
Sine–Gaussian – 393 Hz
Number of triggers
Time [s]

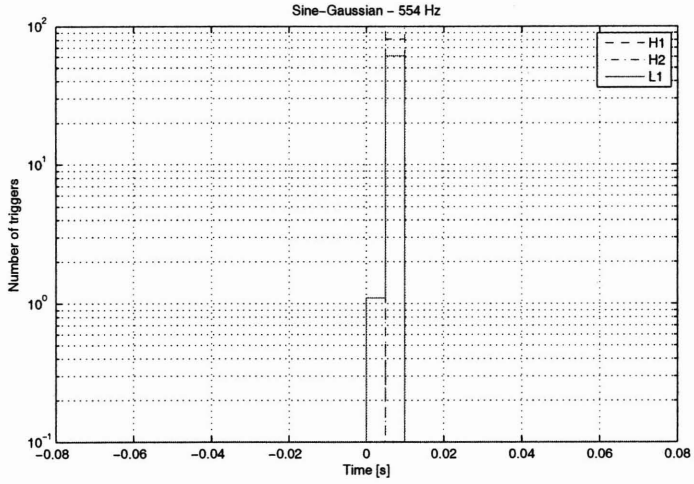
Sine–Gaussian – 554 Hz
H1
H2
L1
Number of triggers
Time [s]

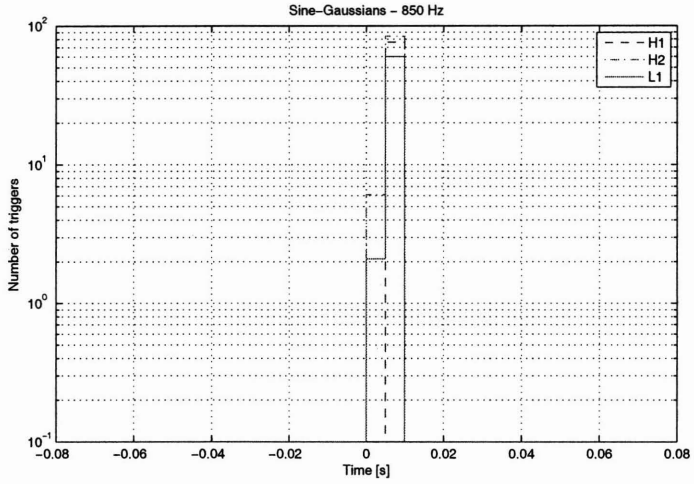
Sine–Gaussians – 850 Hz
H1
H2
L1
Number of triggers
Time [s]

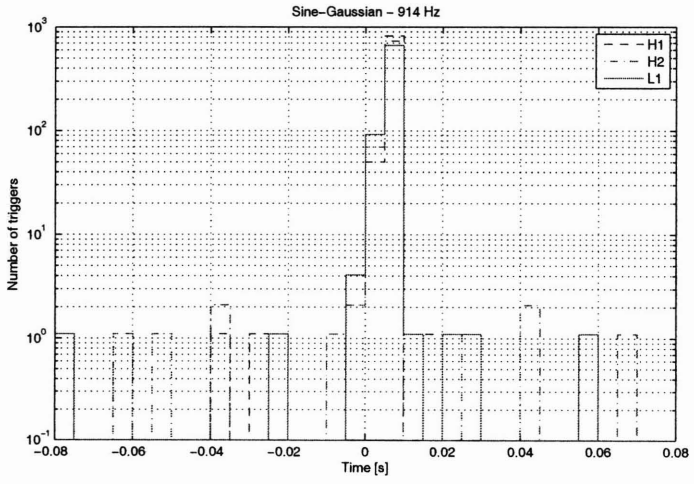
Sine–Gaussian – 914 Hz
H1
H2
L1
Number of triggers
Time [s]

- Astrophysical waveforms

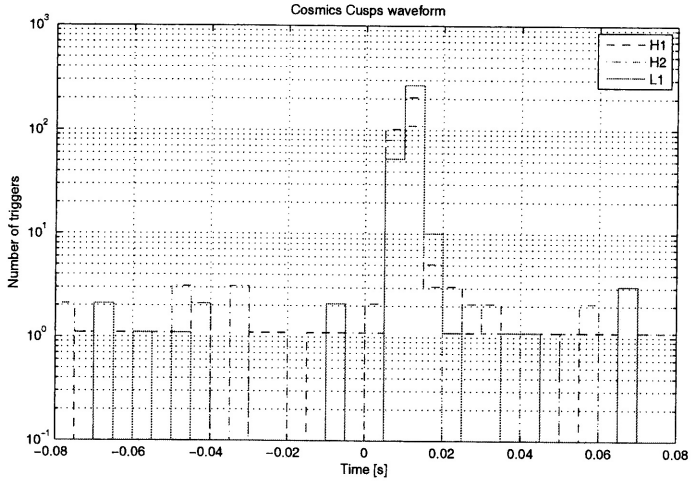

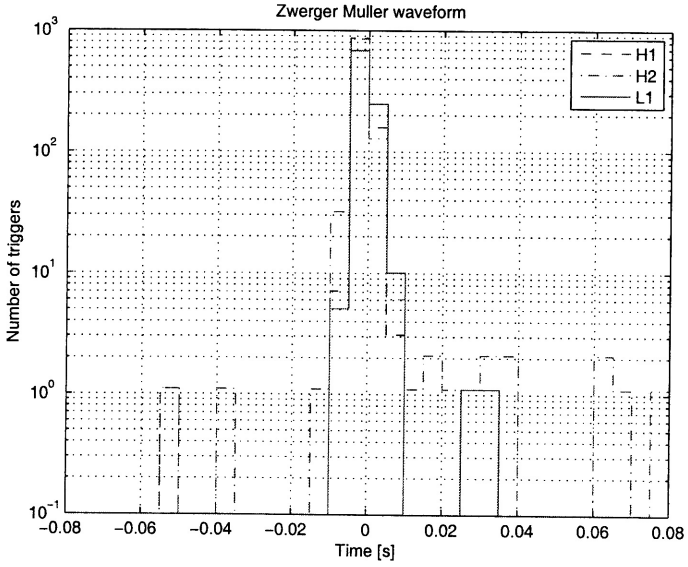

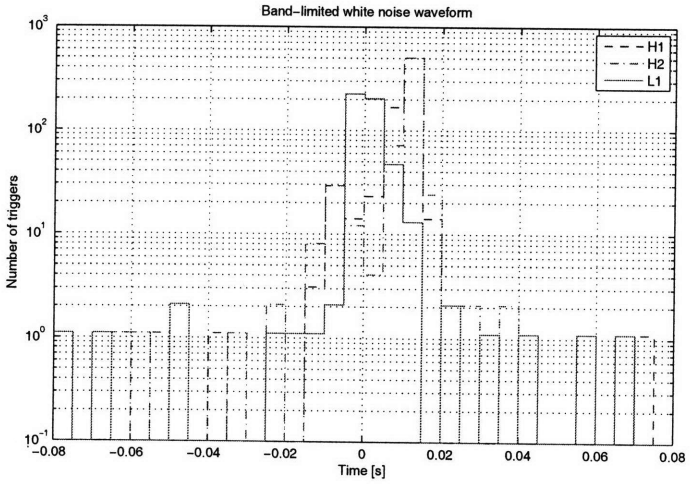
Band–limited white noise waveform
H1
H2
L1
Number of triggers
Time [s]
10^3
10^2
10^1
10^0
10^{-1}
−0.08
−0.06
−0.04
−0.02
0
0.02
0.04
0.06
0.08

Appendix B

Evolution of the efficiency throughout S5

Gaussian 1 ms

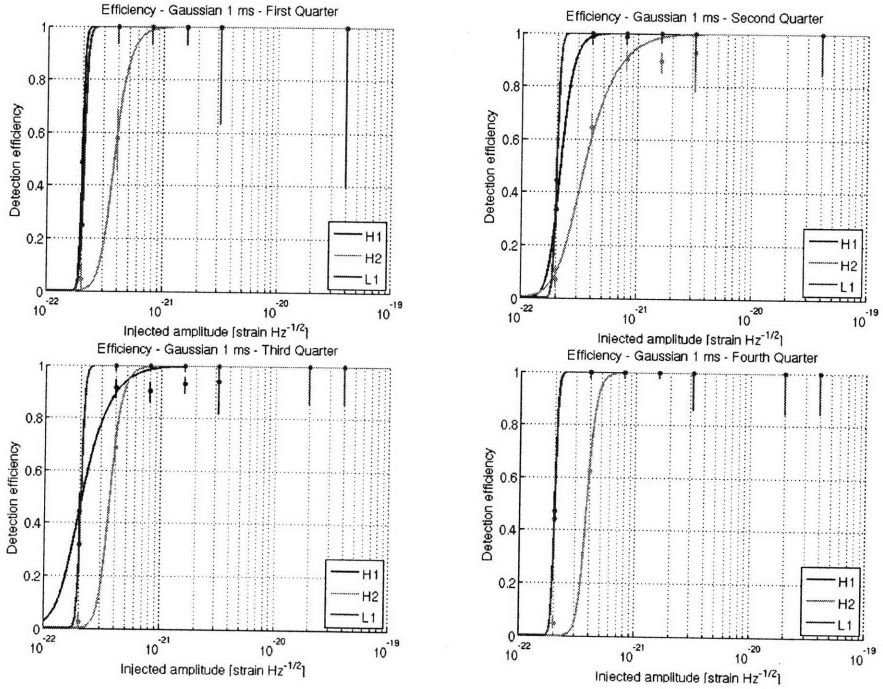

Sinegaussian 70 Hz

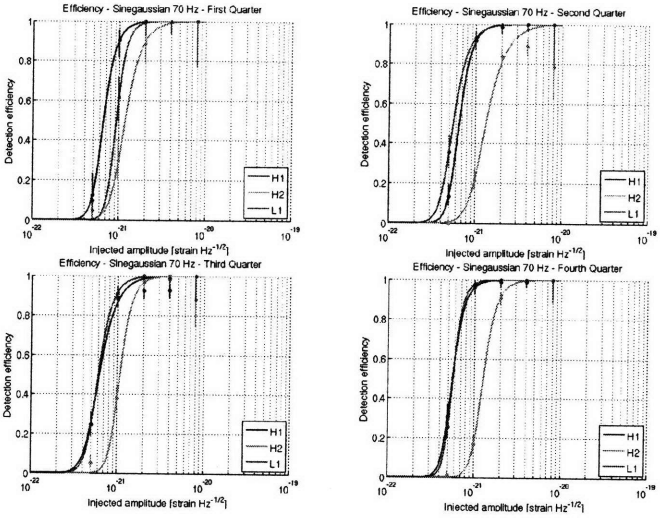

Cosmic String Cusps

For this waveform, we observe that the injected hrss changed during the second quarter of the run. They were indeed too low at the beginning of the run, which explains why the H2 fit was not efficient.

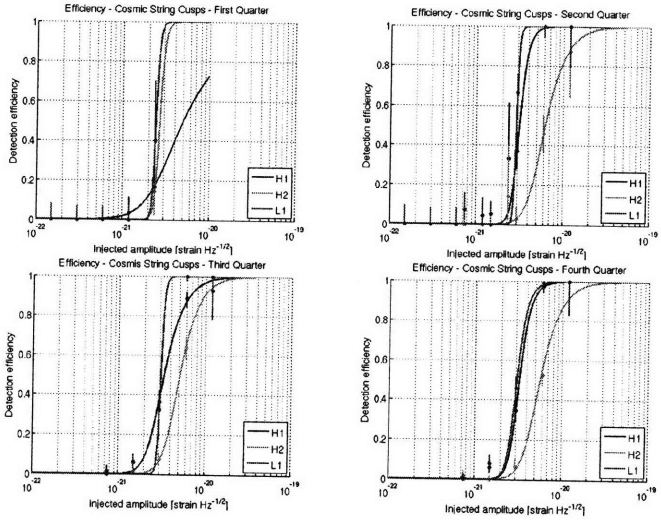

Zwerger Muller waveform

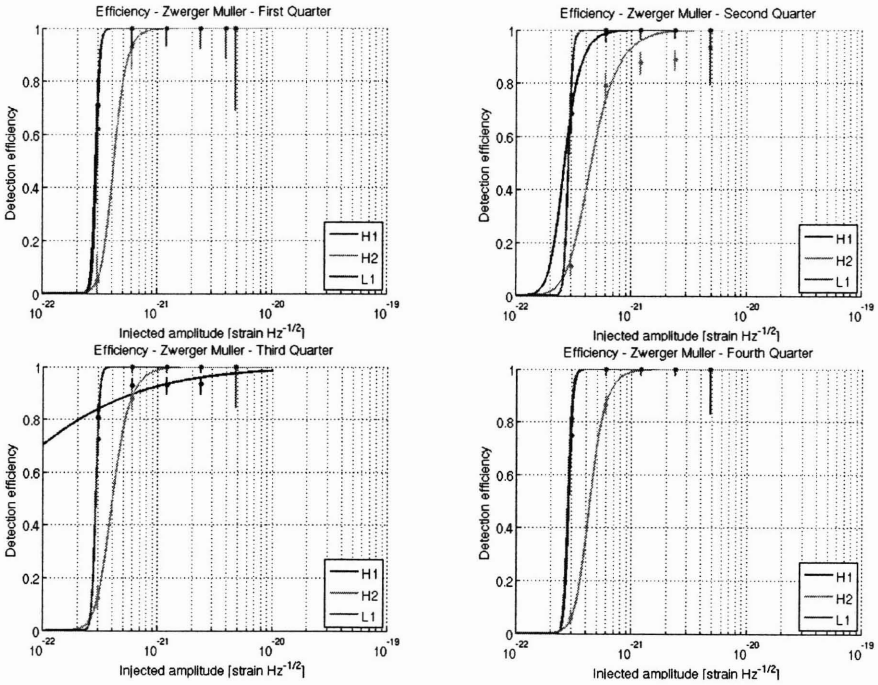

Appendix C

Post S5 Efficiencies

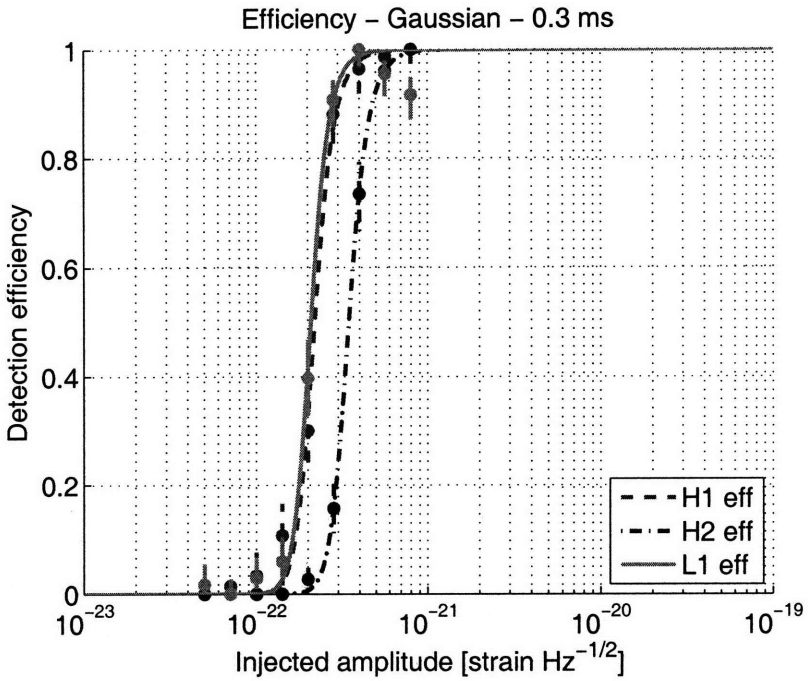

Figure C-1: Dection efficiency of the Gaussian 0.3 ms waveform on October 7th

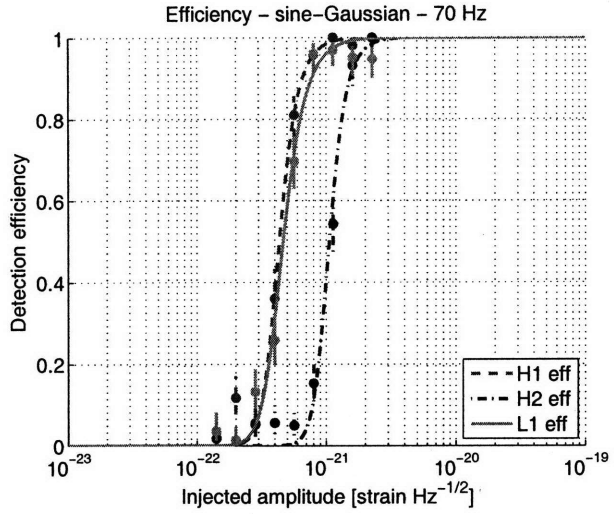

Figure C-2: Dection efficiency of the Sinegaussian 70 Hz waveform on October 7th

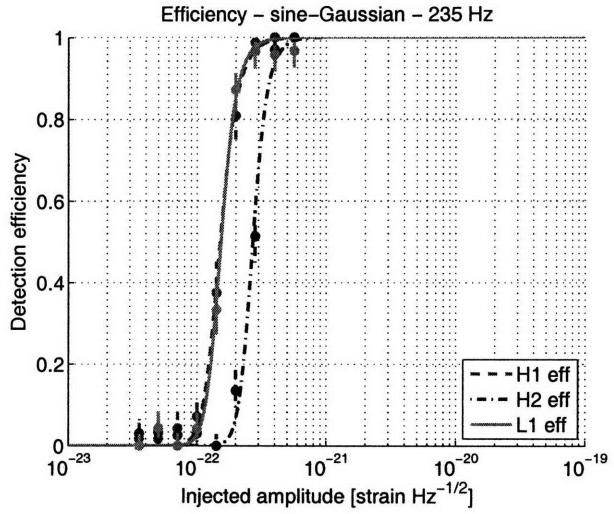

Figure C-3: Dection efficiency of the Sinegaussian 235 Hz waveform on October 7th

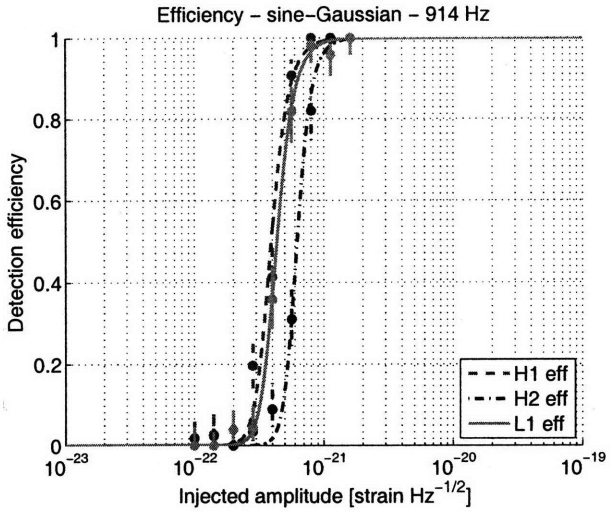

Figure C-4: Dection efficiency of the Sinegaussian 914 Hz waveform on October 7th

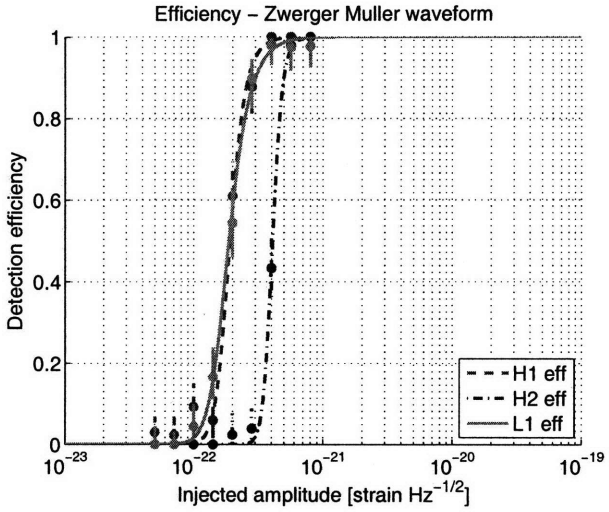

Figure C-5: Dection efficiency of the Zwerger Muller waveform on October 7th

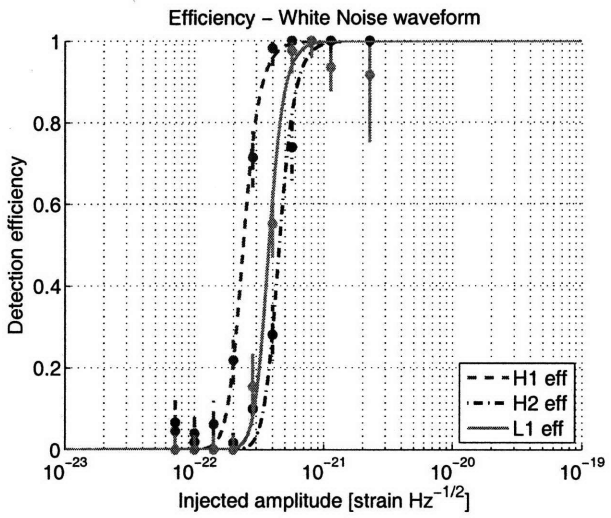

Figure C-6: Dection efficiency of the White Noise waveform on October 7th

Bibliography

[1] R. A. Hulse and J. H. Taylor. *Discovery of a pulsar in a binary system.* Astrophys. J., vol. 195, pp. L51L53, 1989.

[2] J. Weber. *Detection and generation of gravitational waves.* Physical Review, vol. 117, p. 306, 1960.

[3] Samuel J Waldman (for the LSC). *Status of LIGO at the start of the fifth science run.* http://www.iop.org/EJ/abstract/0264-9381/23/19/S03/, 2006.

[4] P. R. Saulson. *Fundamentals of Interferometric Gravitational Wave detectors.* World Scientific Publishing, 1994.

[5] Kip Thorne Curt Cutler. *An overview of Gravitational Wave Sources.* arXiv:gr-qc/0204090v1, 2002.

[6] E. Coccia F. Dubath and M. Maggiore. *On the possible sources of gravitational wave bursts detectable today.* Phys. Rev. D, vol. 70, p. 084010, gr-qc/0405047, 2004.

[7] A. Burrows et al. *On the nature of core collapse supernova explosions.* Astrophys. J. 450:830, 1995.

[8] B. Abbott et al for the LSC. *Search for gravitational-wave bursts in LIGO's third science run.* Classical and Quantum Gravity, 2006.

[9] F. Beauville et al. *A comparison of methods for gravitational wave burst searches from LIGO and Virgo.* Classical and Quantum Gravity, 2008.

[10] K. Thorne. *Gravitational radiation.* Cambridge University Press, 300 Years of Gravitation (S. Hawking and W. Israel, eds.), 1987.

[11] Daniel Sig. *Gravitational Waves.* LIGO-P980007-00 D, 1998.

[12] E. E. Flanagan and S. A. Hughes. *The basics of gravitational wave theory.* New Journal of Physics, vol. special issue: Spacetime 100 Years Later gr-qc/0501041, 2005.

[13] *LIGO Home Page.* http://www.ligo.caltech.edu/.

[14] Igor Yakushin et al. *MDC Frames for S2 Burst Analysis.* LIGO-T040042-00-Z-00-D, 2004.

[15] Lazzarini A and Weiss R. *LIGO Science Requirements Document.* LIGO DCC Number, LIGO-E950018-02-E, 1996.

[16] T. Zwerger and E. Mueller. *Dynamics and gravitational wave signature of axisymmetric rotational core collapse.* Astron. Astrophys., vol. 320, pp. 209227, 1997.

[17] X. Siemens K. Olum. *Cosmic string cusps with small-scale structure: Their forms and gravitational waveforms.* Physical Review, D 68, 085017, 2003.

[18] Lisa M Goggin (for the LIGO Scientific Collaboration). *Search for black hole ringdown signals in LIGO S4 data.* CLASSICAL AND QUANTUM GRAVITY, stacks.iop.org/CQG/23/S709, 2006.

[19] M. Sung for the LSC. *Matched filter analysis of burst waveform injections.* Class. Quantum Grav. 24 (2007) S423S431.

[20] A. Dietz et al. *Calibration of the LIGO detectors for S4.* LIGO-T050262-01-D.

[21] S. Chatterji L. Blackburn G. Martin and E. Katsavounidis. *Multiresolution techniques for the detection of gravitational-wave bursts.* Class. Quantum Grav., vol. 21, pp. S1809S1818, grqc/0412119, 2004.

[22] Lindy Blackburn. *KleineWelle Technical Document.* http://emvogil-3.mit.edu/ lindy/kleineWelle/doc/kwdoc.pdf.

[23] *Upper limits on gravitational-wave bursts in LIGO 's second science run.* LIGO-P040040-07-R.

[24] *Search for gravitational wave bursts in LIGOs third science run.* arXiv:gr-qc/0511146v1/.

[25] *Search for gravitational-wave bursts in LIGO data from the fourth science run.* PACS numbers:04.80.Nn, 95.30.Sf, 95.85.Sz.

[26] A.Dietz et al. *Calibration of the LIGO detectors for S4.* LIGO-T050262, 2005.

[27] *Ligo Sensitivities web-site.* http://www.ligo.caltech.edu/ jzweizig/distribution/LSC Data/.

[28] C. Ott et al. *A new mechanism for gravitational-wave emission in core-collapse supernovae.* American Physical Society, 2006.

[29] Baker Centrella Choi Koppitz and van Meter. *Binary black hole merger dynamics and waveforms.* J 2006 Phys. Rev, D 73 104002, 2006.